MOX-Report No. 52/2016

The 3D Numerical Simulation of Near-Source Ground Motion during the Marsica Earthquake, Central Italy, 100 years later

Paolucci, R.; Evangelista, L.; Mazzieri, I.; Schiappapietra, E.

MOX, Dipartimento di Matematica
Politecnico di Milano, Via Bonardi 9 - 20133 Milano (Italy)

mox-dmat@polimi.it http://mox.polimi.it

The 3D Numerical Simulation of Near-Source Ground Motion during the Marsica Earthquake, Central Italy, 100 years later

R. Paolucci[1], L. Evangelista[2], I. Mazzieri[3], E. Schiappapietra[4]

ABSTRACT

In this paper we show 3D physics-based numerical simulations of ground motion during one of the most devastating earthquakes in the recent Italian history, occurred on Jan 13, 1915, Marsica, Central Italy. The results provide a realistic estimate of the earthquake ground motion and fit reasonably well both the geodetic measurements of permanent ground settlement, and the observed macroseismic distribution of damage. In addition, these results provide a very useful benchmark to improve the current knowledge of near-source earthquake ground motion, including evaluation of the best distance metrics to describe the spatial variability of the peak values of ground motion, the relative importance of fault normal vs fault parallel components, the conditions under which vertical ground motion may prevail, as well as the adequacy of 1D vs 3D modelling of site amplification effects.

1. Introduction

100 years ago, on January 13, 1915, at 6:52 local time, a catastrophic earthquake devastated Marsica, Southern Abruzzi, Central Italy, causing around 33,000 fatalities. Among the most important municipalities hit by the earthquake, the ruin of Avezzano was complete, with 10,700 fatalities, 95% of the total population [1]. A single reinforced concrete building in Avezzano, one of the very first ones constructed at those times, withstood the earthquake and was later declared national monument. Unfortunately, since Italy was about to enter World War I, the government minimized the effects of the earthquake and denied the international support which was a key for recovery after the Reggio-Messina catastrophe of December 28, 1908, only 4 years before. Therefore, the rescue operations were dramatically slow and some further 3,000 fatalities were estimated because of post-earthquake diseases.

The earthquake was felt up to several hundred km distance: for example, in Rome, about 80 km W of the epicentre, the I_{MCS} intensity was estimated from VI to VII. A sketch of the MCS intensities through the Southern Abruzzi region, together with the surface projection of the fault and the location of the instrumental epicentre is illustrated in Fig. 1.

The earthquake was originated by the Fucino fault system [2] consisting of an array of NW-SE striking normal faults, dipping mainly SW, which is also attributed to have generated the

1 Professor, Dept. Civil and Environmental Engineering, Politecnico di Milano, Italy, roberto.paolucci@polimi.it

2 Researcher, Institute for Coastal Marine Environment (IAMC), National Research Council (CNR), Naples, Italy, lorenza.evangelista@cnr.it

3Post-doc researcher, MOX - Laboratory for Modeling and Scientific Computing, Department of Mathematics, Politecnico di Milano, Milan, Italy, ilario.mazzieri@polimi.it

4National Dept. of Civil Protection, Roma, Italy, erika.schiappapietra@gmail.com

earthquake which severely affected Rome in 508 AD [3]. While clear evidence of the surface fault rupture was pointed out by the post-earthquake survey by Oddone [4], who followed the fault trace from SE to NW for about 33 km, there is no consensus on the epicentre location. On the one side, this is often reported, such as in [1], to be located at the center of the maximum intensity macroseismic area, roughly coinciding with the center of the Fucino basin. On the other side, an instrumental determination was proposed by [5], and also reported by [6] in a special volume dedicated to the Marsica earthquake, based on the available seismometer recordings, which lead to the location 41.975 N – 13.605 E, which has been used in this paper and is shown in Fig. 1. Different determinations of the earthquake magnitude are also reported in the literature, and reviewed by [6], leading to Ms evaluations ranging from 6.6 to 7.0.

The presence of a prevailing normal faulting system, bordering a tectonic basin, is one of the key features of seismogenic activity in the Central-Southern Apennines, and poses the key problem of coupling the presence of the seismic fault with soft sedimentary basins, having relatively young age and large thickness, thus enhancing the hazard typical of near-source conditions.

In this research, we have simulated near-source ground motion during the Marsica earthquake, taking advantage of the SPEED code, developed at Politecnico di Milano to perform 3D physics-based numerical simulations of seismic wave propagation. These include a kinematic model of the seismogenic fault rupture and a 3D model of the shallow crustal layers, including the complex geological irregularity of the Fucino basin.

Different objectives were pursued during this work, namely: (1) providing numerical results suitable to constrain the physical parameters of the earthquake, also by verifying the simulated permanent ground displacements against the vertical settlement estimated by post-earthquake ground level measurements; (2) verifying possible conditions of directivity and interaction with the soft deposits of the Fucino basin, in order to explain the vast devastation in Avezzano, at the Northern edge of the basin, at some 20 km NW of the epicentre; (3) quantifying some relevant parameters of ground motion in near-source conditions, such as the ratio of strike fault normal (FN) vs fault parallel (FP) and the vertical vs horizontal components, as well as their spatial variability; (4) evaluating the best distance metrics to model the peak values of ground motion in near-source conditions; (5) evaluating the adequacy of 1D modelling of site amplification effects in near-source.

2. Geological and Geotechnical Characterization

2.1 Geological framework and geotechnical characterization of Fucino basin

The Fucino basin is the most important intra-mountain depression of the Central Apennines, related to the extensional regime of NW–SE trending normal faults, surrounded by high carbonate ridges of Meso-Cenozoic age. It covers an area of about 900 km^2, of which 200 km^2 are an ancient lake, drained in 1875. The latter was the last stage of a long geologic evolution started in the Pliocene, during which the area was always lower than the surrounding Apennines, interested by uplift movements. The current geological setting of the Fucino basin, illustrated by the geological map and cross-section drawn in Fig. 2, results from a complex sequence of depositional events, due to erosion and tectonics.

The bedrock consists of Meso-Cenozoic carbonate, generally covered by terrigenous Neogene flysch deposits but also outcropping along the sides of the basin. The bottom of the

basin was filled during the Quaternary with continental deposits of variable genesis and deposition age, resulting from lacustrine to subsequent alluvial sedimentations. In detail, the sedimentary sequences were divided [7] into:

- a Lower Unit (Plio-Pleistocene), outcropping on the North-eastern border of the basin, that mainly consists of breccias and alluvia, with subordinate lacustrine deposits;
- an Upper Unit (Upper Pleistocene-Holocene), made up of interdigitated lacustrine and alluvial deposits, that at the border of the depression evolves into alluvial fan deposits, which may even be coarse-grained.

Finally, the Quaternary sedimentary sequence is closed by thick lacustrine deposits in the center of the basin [8].

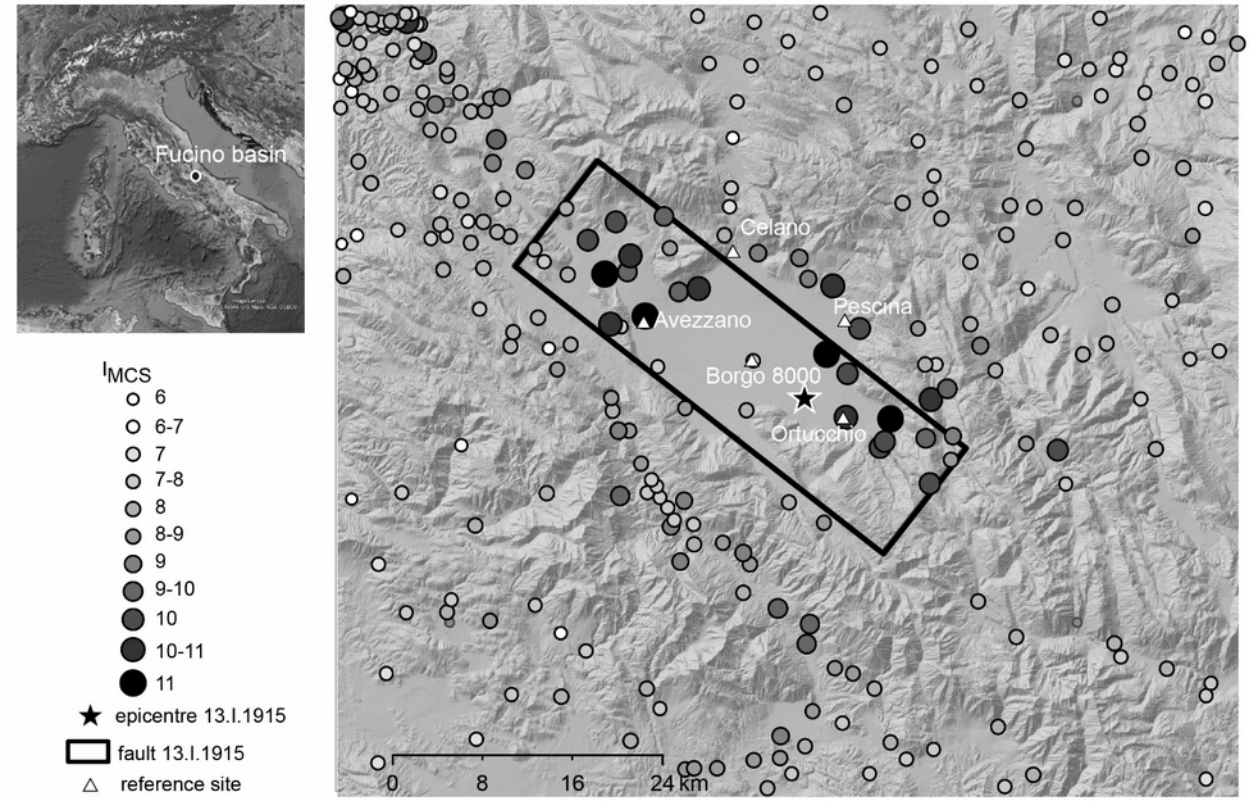

Fig. 1. I_{MCS} distribution according to the Italian macroseismic database [9], including the epicenter and the surface projection of the fault adopted in this work.

This geomorphological setting is the result of a post-orogenic relaxing phase of the central part of Apennines, whose normal fault systems, with NW-SE and E-W-trending high-angle and S-SW-dipping, developed extensional basins along the south-western sector of the overthrust belt [10].
The complex geologic structure is characterized by the overlap, through two separate phases, of two semi-graben; the first one fully developed during the Pliocene, while the second one developed in the Plio-Pleistocene. In Fig. 2a, the isochron map in two-way time (TWT) of lacustrine deposits from seismic profiles is reported. The map shows the presence of a first sub-basin felt in the North sector near Avezzano, with TWT equal to 250 ms, and a second

well defined depocentre near San Benedetto, the so-called Bacinetto, characterized by TWT of 900 ms. Assuming the P-wave velocity for bedrock V_P = 2000 m/s [11], it is possible to derive that the first sub-basin near Avezzano reaches a depth of 250 m, while the deeper one, corresponding to the Bacinetto, is characterized by a maximum depth of 900m.

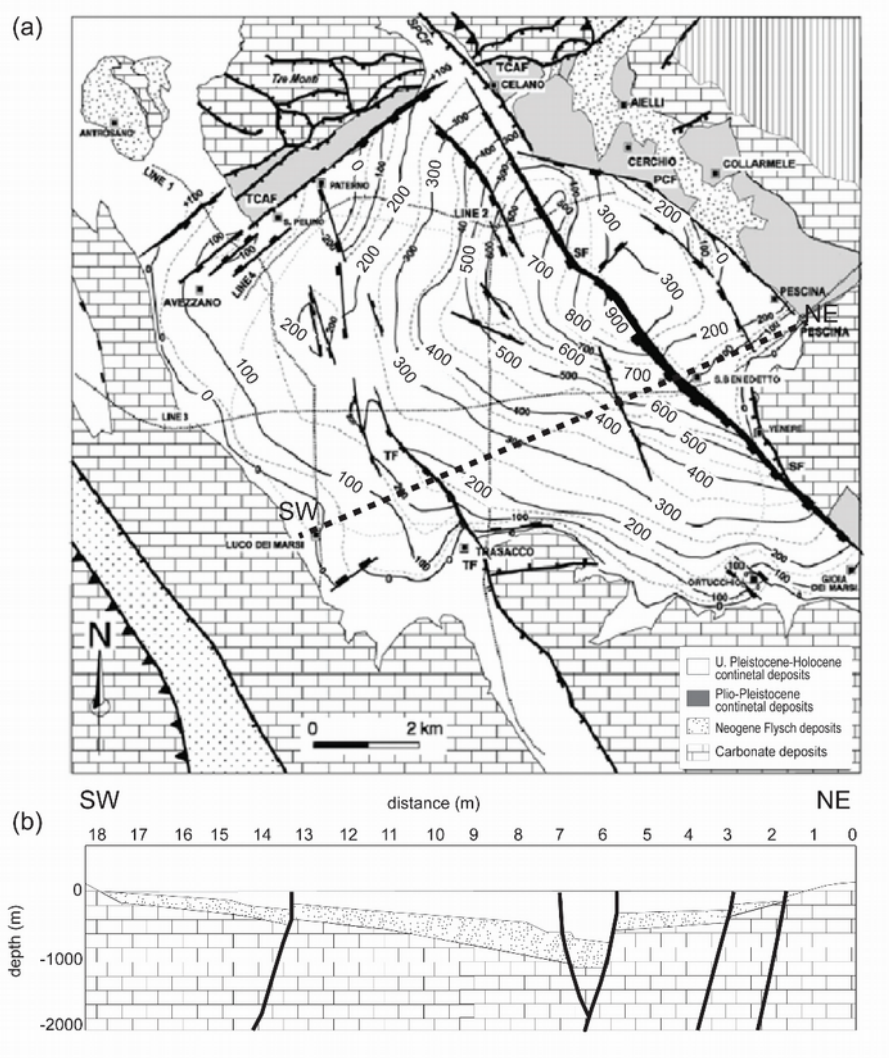

Fig. 2. (a) Geological map and isochron contour map (interval 50 ms and 100 ms) of the alluvial and lacustrine deposits (adapted from [7]); (b) Geological cross-section (from [11]), along the dashed line shown in the top.

The lacustrine deposits, filling the latter sub-basin, were involved by an extensive geotechnical characterization activity in 1986 [12] to evaluate the dynamic subsoil properties. The specific investigations, planned for the geotechnical characterization, consisted of in situ tests, including Cross-Hole (CH), Down-Hole (DH), Flat Dilatometer Test (DMT) and Spectral Analysis of Surface Waves (SASW), and of a laboratory program with Resonant Column (RC) and Torsional Shear (TS) tests. Fig. 3a shows the comparison of the in situ shear wave velocity (V_S) profiles. The data from different sources show a good agreement within the investigation depth and a significant increase of V_S with depth. Since the in situ tests investigated only down to the first 40m (Fig. 3a), the increase of V_S profile along the whole thickness of lacustrine deposits was described by scaling the law of variation of the small strain shear modulus (G_0) with the mean effective stress (p') measured in RC-TS tests

(Fig. 3a). To this aim, the variation of G_0 with p' observed in the RC-TS tests, was first expressed in terms of shear wave velocity, V_S (white squares in Fig. 3a), as a function of depth. The latter was related to p' by assuming a coefficient of earth pressure at rest $k_0 = 0.8$, that is the mean along the depth as evaluated by DMT tests [12].

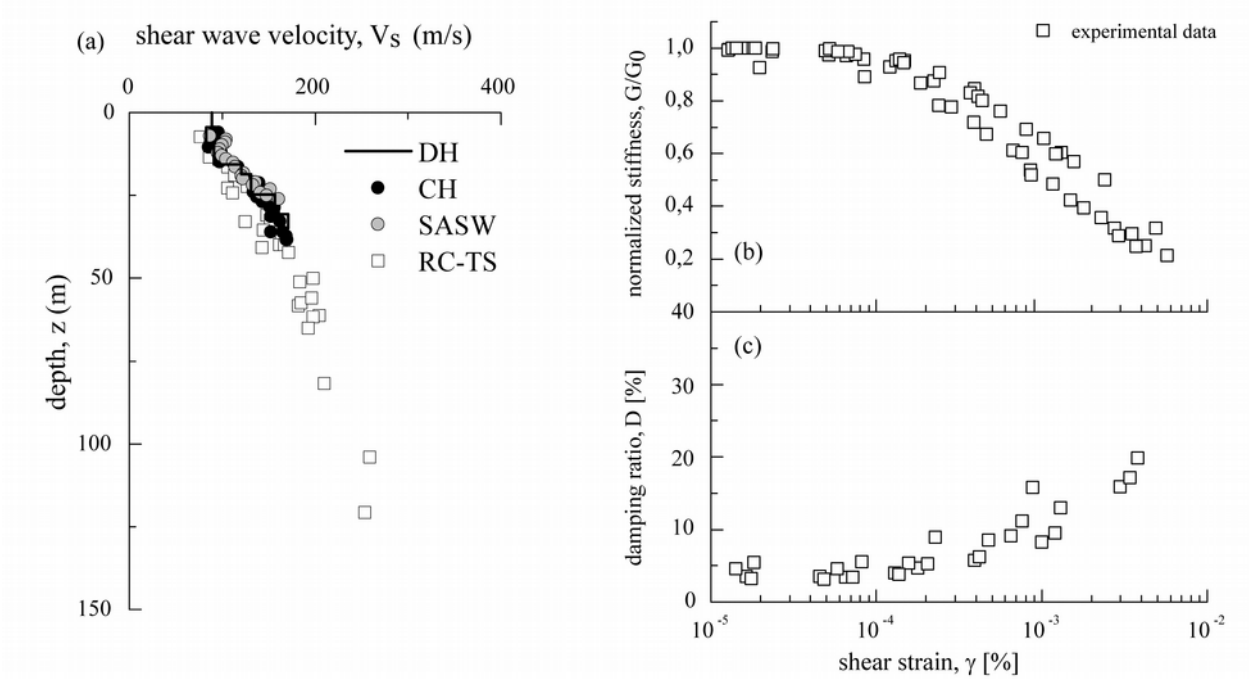

Fig. 3. (a) Comparison of shear wave velocity profiles obtained by DH, CH, SASW and RC-TS; Normalised shear modulus (b) and damping ratio (c) versus shear strain from RC-TS tests.

The RC-TS tests confirmed the significant increase of V_S along the thickness of lacustrine deposits and allowed obtaining a shear wave velocity profile down to 100 m.

The non-linear behavior of the lacustrine deposits, typical consisting of medium-high plasticity clays, was modeled based on the results of laboratory tests, reported in Fig. 3b-3c, in terms of variation of the normalized shear modulus, G/G_0, and of the damping ratio, D, versus the shear strain, γ. These curves were implemented in the 3D numerical code [13] by introducing a scalar measure of shear strain amplitude:

$$\gamma_{max}(\boldsymbol{x},t) = max\left[\left|\varepsilon_I(\boldsymbol{x},t) - \varepsilon_{II}(\boldsymbol{x},t)\right|, \left|\varepsilon_I(\boldsymbol{x},t) - \varepsilon_{III}(\boldsymbol{x},t)\right|, \left|\varepsilon_{II}(\boldsymbol{x},t) - \varepsilon_{III}(\boldsymbol{x},t)\right|\right] \quad (1)$$

where ε_I, ε_{II} and ε_{III} are the principal values of the strain tensor. Once the value of γ_{max} is calculated at the generic position $\boldsymbol{x}$ and generic instant of time t, its effective value (set as $0.6\gamma_{max}$) is introduced in the G-γ and D-γ curves to update the corresponding values for the following time step. Therefore, unlike the classical linear-equivalent approach, in this non-linear elastic approach the initial values of damping and stiffness are recovered at the end of the excitation.

2.2 Construction of a numerical model

The numerical model of the Fucino basin extends over an area of 56x46x20 km^3 (Fig. 4). It is built by assembling the topographic layer, obtained by a 250 m Digital Elevation Model, with the underlying layers describing the bedrock morphology as provided by seismic profiles [7]. The fault geometry is also included into the model, as it will be discussed in the following section.

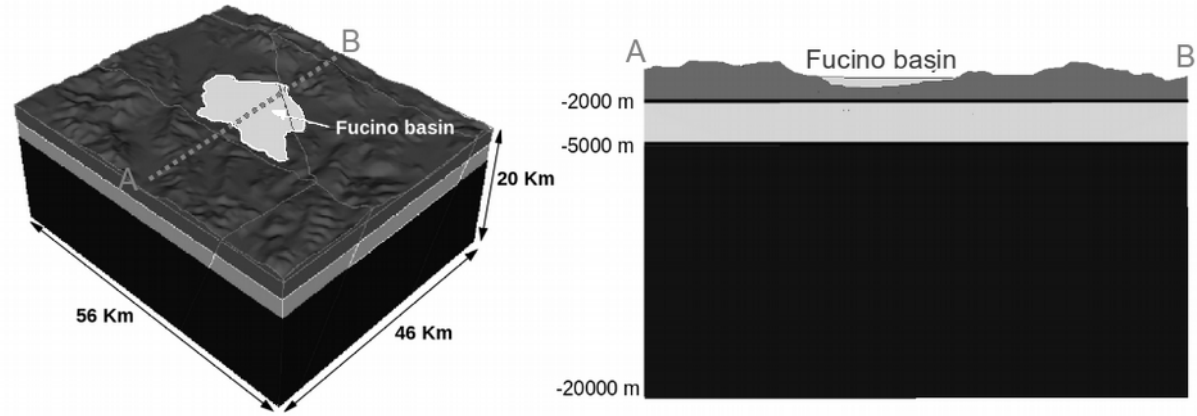

Fig. 4. 3D numerical domain, with a representative cross-section, transverse to the Apennine chain.

The morphology of the buried bedrock is derived by the interpretation of seismic profiles shown in Fig. 2. According to the geotechnical characterization described in the previous section, the lacustrine sediments are assumed to behave as a non-linear visco-elastic medium, characterized by a single profile of density (ρ) and shear wave velocity (V_S), as follows:

$$\rho(z) = 1530 + 10 \cdot z^{0.54} \ \text{(kg/m}^3\text{)} \tag{2}$$

$$V_S(z) = 180 + 10 \cdot z^{0.60} \ \text{(m/s)} \tag{3}$$

where z is depth, expressed in m.

The model of V_S is in good agreement with those derived by [11] from experimental measurement of resonance frequency by standard spectral ratio (SSR) and horizontal-vertical spectra ratio (HVSR) methods. The V_P values were based on the corresponding V_S, by considering a Poisson ratio $\nu = 0.44$, estimated from the coefficient of earth pressure at rest $k_0 = 0.8$ based on DMT tests [12]. The quality factor Q was assumed to be proportional to frequency ($Q = Q_0 f/f_0$), where $Q_0 = V_S/10$ is the value at $f_0 = 0.5$ Hz.

Outside the basin, a crustal model is adopted based on [14]. It is characterized by five horizontal and parallel layers resting on a half-space at a depth of 20 km. In particular the V_S values of the shallow layers have been reduced with respect to those of [14], in agreement with the site investigations [15], in order to decrease the basin-to-rock impedance ratio. The properties of each layer are shown in Table 1.

Table 1

Horizontally stratified crustal model assumed for the 3D numerical simulations.

H (m)	V_S (m/s)	V_P (m)	ρ (kg/m^3)	Q
500	1000	1800	2300	100
1000	1700	3160	2500	150
2000	2600	4830	2840	250
5000	3100	5760	2940	300
20000	3500	6510	3180	350

It is finally pointed out that no consideration of other specific geological conditions was made out of the boundaries of the Fucino basin. Therefore, numerical results outside the Fucino basin are representative of outcropping bedrock conditions and cannot be directly used to quantify ground motion in surrounding valleys, such as Valle del Liri, SW of the basin, which was also dramatically affected by the earthquake (see Fig. 1).

3. Kinematic modeling of the seismic source

There is a general consensus that the Marsica earthquake was generated along the Fucino system of normal faults [3], which borders on the Eastern side the Fucino basin, the strike of which is aligned along the Apennines chain. This indication is well constrained by different sources, such as by the post-earthquake survey of Oddone [4], who clearly witnessed the evidence of the line formed by the surface fault rupture, extending about 30 km from SE to NW, by the downward settlements of the 18 geodetic benchmarks (monumental statues) placed around the Fucino lake before drainage in 1875, on the hanging wall side of the rupture [16-18], and by the numerous paleoseismological studies in that area ([19], [2-3]).

The set of fault parameters considered in our numerical simulations is summarized in Table 2, while the slip distribution is illustrated in Fig. 5. We mainly based the geometric parameters (dimensions, position, strike, dip, rake) on Galadini (personal communication, 2015), the slip distribution on [16], and the epicentre on the instrumental location by [5]. By modulating the amplitude of slip distribution, we considered a range of M_W from 6.7 to 7. The value M_W 6.7 reported in Table 2 is the one for which the best agreement was obtained with the benchmark settlements, as discussed later. Further slip distributions corresponding to M_w6.7 were considered, as investigated by [20], but providing less satisfactory results than obtained with the one introduced in this paper.

4. Numerical modeling of seismic wave propagation by Spectral Elements

4.1 SPEED: Spectral Elements in Elastodynamics with Discontinuous Galerkin

SPEED is a certified numerical software (http://speed.mox.polimi.it) for 3D elastodynamics problems, that is specifically suited to study seismic wave propagation and dynamic soil-structure interaction problems in complex geological configurations. The code is jointly

developed at MOX - Laboratory for Modeling and Scientific Computing of the Department of Mathematics and at the Department of Civil and Environmental Engineering of Politecnico di Milano. The SPEED kernel is based on a discontinuous version of the classical Spectral Element (SE) method, a non-conforming domain decomposition technique combining the flexibility of discontinuous Galerkin finite elements with the accuracy of spectral techniques. Based on the work of [21], the SE approximation described in [22] and [23] has been extended to address discontinuous discretizations.

Indeed, Discontinuous Galerkin Spectral Element (DGSE) approaches are shown to be able to capture local variations of the physical solutions while locally preserving the same accuracy of SE methods in term of dissipation and dispersion errors (see [21]). Moreover, DGSE methods can handle non-matching grids and different local approximation degrees making such schemes much more flexible than classical SE approaches from the mesh generation point of view (at price of an increased computational complexity). Finally, DGSE methods enjoy a high level of intrinsic parallelism, making such a discretization technique well suited for massively parallel computations [24].

Table 2.
Fault parameters adopted in this work.

Fault Parameters	Present study
Fault Origin F_O (Lat, Lon)	(42.15, 13.37)
Top Depth of Fault H_{min} (km)	0.337
Length along Strike L (km)	41.6
Width along Dip W (km)	20
Epicenter (Lat, Lon)	(41.97, 13.60)
Focal Depth (km)	6.4
Strike (°)	127.8
Dip (°)	53.3
Seismic moment M_0 (Nm)	$1.25\ 10^{19}$
Mw	6.7
Rise time τ (s)	0.70
Rupture Velocity V_R (m/s)	0.85 V_S
Rake (°)	260

Fault Geometry

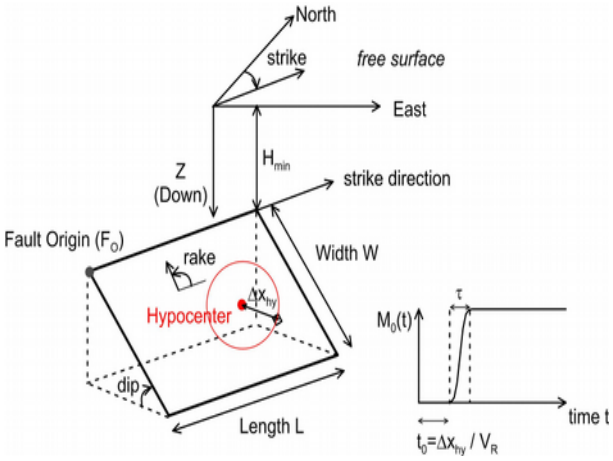

The present version of SPEED includes the possibility to treat seismic wave propagation in linear and non-linear visco-elastic heterogeneous soils, characterized either by frequency proportional quality factor [24], or frequency constant quality factor [25], with non-linear elastic response as described in section 2.1. Paraxial boundary conditions [26] are introduced to reduce spurious reflections from outgoing waves inside the computational domain, while time integration can be performed either by the second order accurate explicit leap-frog scheme or the fourth order accurate explicit Runge-Kutta scheme (see [27]).
Recently, SPEED was successfully applied for the numerical simulation of near-source ground motion during the 2012 Po plain seismic sequence in Italy [28], for hazard assessment analysis in large urban areas for reinsurance evaluations as described in [24], as well as for

city-site interaction problems and for the dynamic response of extended infrastructures [29-30].

4.2 Spectral Element model and numerical performance

The 3D computational domain used for the SPEED simulations was built based on data described in Sections 2 and 3, being a compromise between, on one side, the need to fit as closely as possible the available geological and geophysical information throughout a large spatial region, and, on the other side, to cast such information within a reasonably simple form apt to construct the computational model.

Considering a rule of thumb of 5 grid points per minimum wavelength for non-dispersive wave propagation in strongly heterogeneous media by the SE approach (cfr. [21]), and considering a maximum frequency f_{max} = 2 Hz, the model consists of 464.470 hexahedral elements, resulting in 90.339.030 degrees of freedom, using a fourth order polynomial approximation degree. A conforming mesh was set up, having size ranging from a minimum of 80 m, within the quaternary basin, up to 440 m in the outcropping bedrock, and reaching 1250 m in the underlying layers, see Fig. 5a.

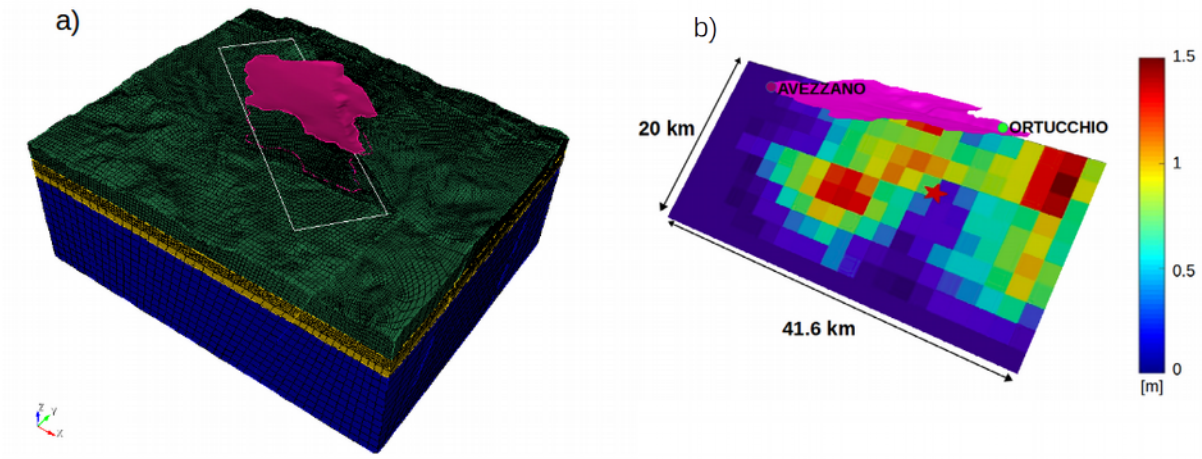

Fig. 5. (a) 3D computational mesh adopted for the numerical model along with the projection of the seismic fault responsible of the January 13 1915 earthquake and buried topography, corresponding to Quaternary sediments in Fig. 2. (b) Assumed slip distribution to model the earthquake fault rupture, as described in Section 3.

A fault plane was introduced in the numerical model (Fig. 5b), complying with the geometric and kinematic features reported in Table 2. At each cell of the fault plane, a slip time history *s(t)* is prescribed in terms of an approximate step function:

$$s(t) = \frac{s_0}{2}\left[1 + erf\left(4\frac{t - t_0 - 2\tau}{\tau}\right)\right] \tag{4}$$

where *erf* (·) is the error function, τ = 0.7 s is rise time, t_0 is the rupture time from the hypocentre to the cell, and the final slip s_0 is mapped in Fig. 5. To enhance the high-frequency radiation, a random variability of rise time and rake angle around their average value is considered, with self-similar spatial correlation [32]. Moreover, to avoid the onset of very high velocity pulses due to super-shear effects, the rupture velocity has been bounded to $V_R = 0.85V_S$, being V_S the shear wave velocity at the corresponding source depth. More advanced approaches to account for the spatial variability of the slip field on the fault, such as the self-similar model introduced by Herrero and Bernard [31], already implemented in SPEED and used for the numerical simulations of the 2012 Po Plain earthquake [28], are expected to provide an even more realistic excitation of the high-frequency range of wave motion. However, we did not introduce such approach in this paper, to keep the slip distribution as close as possible to that of Ward and Valensise [16], that we used as a reference for this paper.

For the numerical simulations the time integration has been carried out with the explicit second order accurate leap-frog scheme, choosing a time step Δt = 0.2 ms for a total observation time T = 50 s. The simulations have been carried at the Gigat cluster located at MOX-Laboratory for Modeling and Scientific Computing, Department of Mathematics, Politecnico di Milano (http://hpc.mox.polimi.it/hardware/) using 32 parallel CPUs, resulting in a total computation time of about 194 hours for a single simulation.

5. Discussion of results

5.1 Permanent vertical settlements

We have first verified the adequacy of the fault geometry and of the slip distribution model by comparing the simulated vertical displacements with the post-earthquake geodetic measurements performed by Loperfido [32] (values taken from [17]). In Fig. 6a, the map of permanent vertical ground displacements is reported, together with the location of geodetic benchmarks. The comparison is shown in Fig. 6b for two values of M_W, obtained by changing the amplitude of slip distribution. The best agreement was found for M_W 6.7, compatible with the best solution of [18] who found the minimum misfit with M_W 6.6±0.1.

As reported by [18], Loperfido himself underlined that some measurements might have been inaccurate, as benchmark 6, which was pulled off by the earthquake, and benchmark 11, lying on marshland and possibly subjected to additional ground settlements.

It should be finally pointed out that the numerical code cannot model permanent fault offsets through elasto-plastic approaches, since, as discussed in section 2.1, the constitutive soil modelling is based on a simplified non-linear visco-elastic behaviour. Therefore, the final settlements computed by the code are of elastic nature, being the ground surface expression of the fault offsets imposed along the fault through the slip map illustrated in Fig. 5.

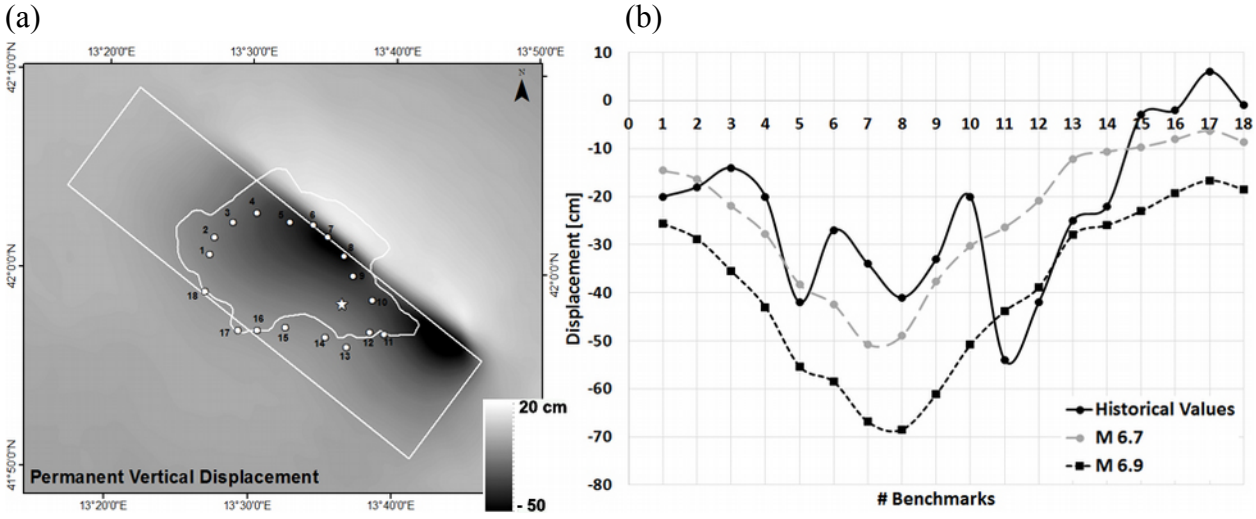

Fig. 6. (a) Map of permanent vertical displacements computed by SPEED for a simulated earthquake magnitude Mw 6.7, with the slip distribution in Fig. 5. (b) Comparison of the historical values from ground levelling measurements [33] (black line), with the simulated permanent displacements obtained with Mw 6.7 (grey line) and Mw 6.9 (black dot line).

5.2 Fault Normal and Fault Parallel components

In Fig. 7, snapshots of horizontal ground velocity, rotated in the strike fault normal (FN) and fault parallel (FP) components, are shown. The amplification of motion due to basin effects is very clear. Also, it is worth to remark that, while in the initial phase of motion the FN component is prevailing, as it should be due to the normal faulting assumption (although a very small strike slip component is present, as shown by rake angle = 260°, see Table 2), the FP component becomes very clear inside the basin at about 7 s. This is mainly associated to Rayleigh waves, generated inside the basin, propagating in the NW direction towards Avezzano.

The peak ground velocity (PGV) maps of the FN and FP components, together with the corresponding velocity records, are illustrated in Fig. 8. Here, the observed variability of ground motion is striking, with different features observed on the footwall (Pescina and Celano) and on the hanging wall of the fault (Ortucchio, Borgo8000, Avezzano), probably related to the coupling of different soil conditions and different location with respect to the fault plane. Duration of the strongest portion of ground motion is about 5 s, in very good agreement with the reports of the survivors [4].

It should be noted that the largest PGV values occur close to the edge of the surface projection of the fault plane. However, these values are likely overestimated by our numerical simulations, because the energy dissipation due to the surface fault rupture is not accounted for, although a moderate nonlinear response is considered through a nonlinear elastic model following the curves in Fig. 3b. To underline the difficulty in predicting peak ground motion values in the proximity of the fault, it is worth to remark that the available records during the

M_W 6.7 Fukushima Hamadori, Japan, normal faulting earthquake on April 12, 2011 [33], therefore in similar conditions as in our study, have shown PGV values larger by a factor ranging from 1.4 to 1.8 than the predicted ones by ground motion prediction equations (GMPE).

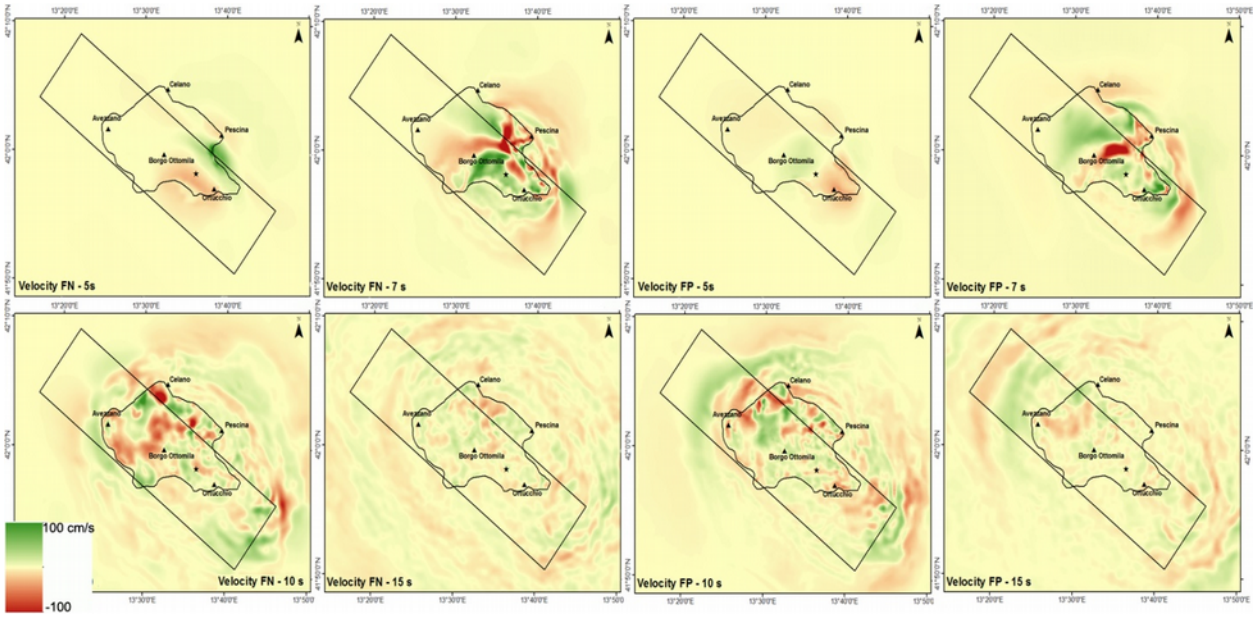

Fig. 7. Snapshots of the computed velocity field at different time instants T = 5, 7, 10, 15 s. (a) Fault Normal (FN) component. (b) Fault Parallel (FP) component.

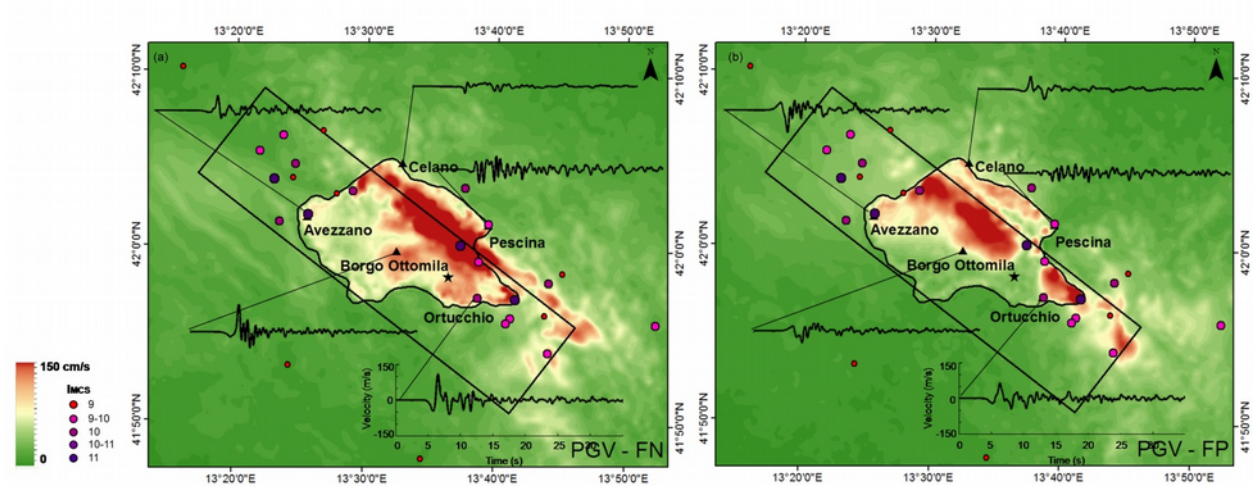

Fig. 8. PGV map for the FN (a) and FP (b) components, together with the corresponding velocity time histories at selected sites (Avezzano, Ortucchio, Pescina, Celano, Borgo Ottomila). Colored dots denote the I_{MCS} grades.

Next, we show in Fig. 9 the spatial distribution of response spectral ratios (5% damped) of the FN vs FP components of motion, for vibration periods T = 0.75 s, 1 s, 2 s. It can be seen that this ratio is by far larger than 1 in the proximity of the surface fault rupture, as expected

for a normal fault. Moving away from the largest asperities of the fault rupture, this ratio decreases to values typically ranging between 1 and 1.5. It is worth noting that, as seen from the right hand side plot on Fig. 9, the FP component tend to dominate at long periods (T = 2 s) close to the NW side of the basin, probably due to the dominance of Rayleigh waves propagating in that direction, as noted previously.

It is also interesting to make a further check with the observation, made by Oddone [4], of the prevailing "azimuth of shaking", i.e., the direction of the strongest shaking based on the observed damage on buildings. One century ago, this was one of the most common ways to estimate the prevailing direction of strong ground motion. Such directions were depicted by Oddone as arrows in the isoseismal plot, based on the original Mercalli scale, that he constructed after the earthquake (Fig. 10). We have highlighted in the same figure the arrows at the localities of Ortucchio, Avezzano and Celano, and superimposed the orbits of ground motion in the horizontal plane. It can be seen that, while in Ortucchio this was recognized to be roughly in the FN direction, both in Avezzano and Celano the evidence of a roughly FP prevailing direction was found by [4], in reasonably good agreement with the numerical simulations.

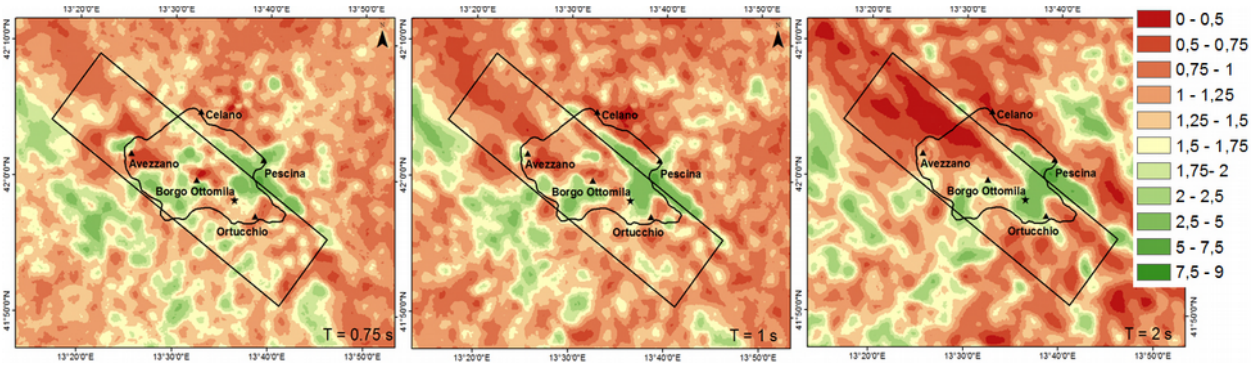

Fig. 9. Spatial distribution of the ratio between FN and FP component of 5% damped response acceleration spectrum for T = 0.75 s (a), 1 s (b), 2 s (c).

5.3 Vertical components of ground motion

Different studies based on near fault records (see e.g., [34-35]) highlighted that the ratio of vertical to horizontal response spectra (V/H) is strongly dependent on period, with V/H values that may be substantially larger than 1 at short periods (T < 0.2 s), but that typically fall to about 0.5-0.6 at longer periods. We have explored the vertical components of ground motion from our simulations, to check whether a similar trend is found, although it should be remarked that the computational frequency limit of our simulations is about 2 Hz.

First, we have plotted in Fig. 11 the vertical PGV map, with a sample of vertical velocity time histories, similarly to Fig. 8, showing consistently large values throughout the basin, especially close to the fault rupture, where the values experienced are similar to the horizontal ones, shown in Fig. 8. Such large impact of the vertical components may be explained in terms of the normal tectonic movement with a major vertical component

involving practically the whole Fucino basin, as shown in Fig. 6.

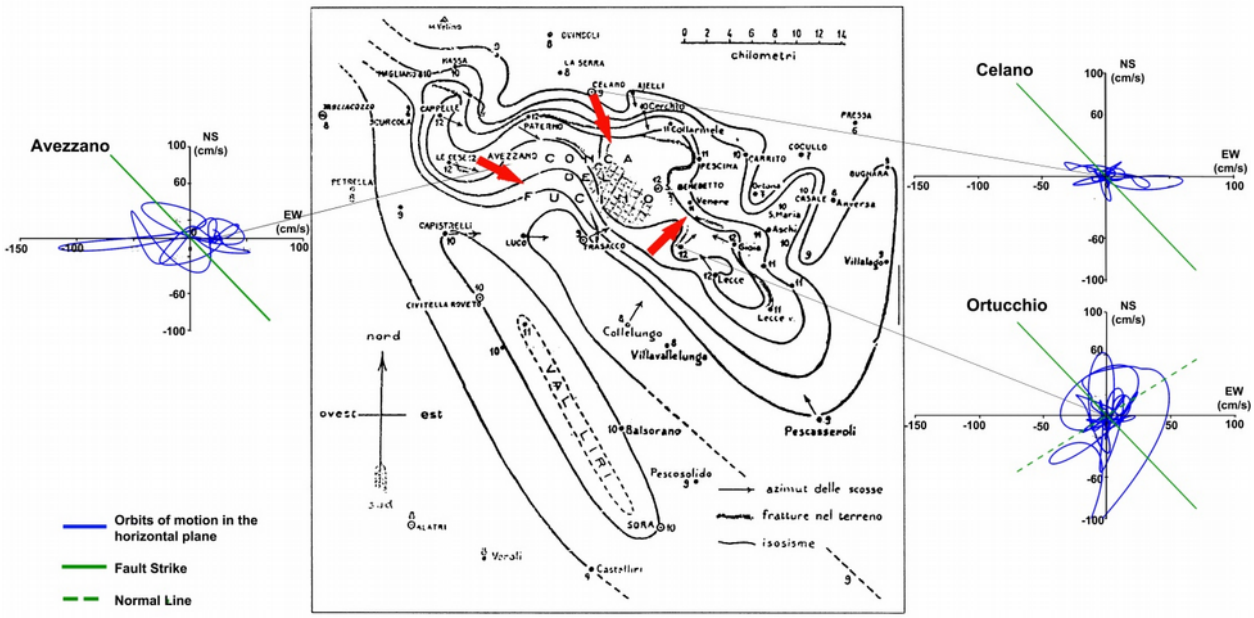

Fig. 10. In the background (figure center), the isoseismal map compiled by [4] after the earthquake, together with the arrows denoting the prevailing "azimuth of shaking". Superimposed are the plots of the orbits of ground motion in the horizontal plane, computed by the numerical simulations, at the sites of Avezzano, Ortucchio and Celano.

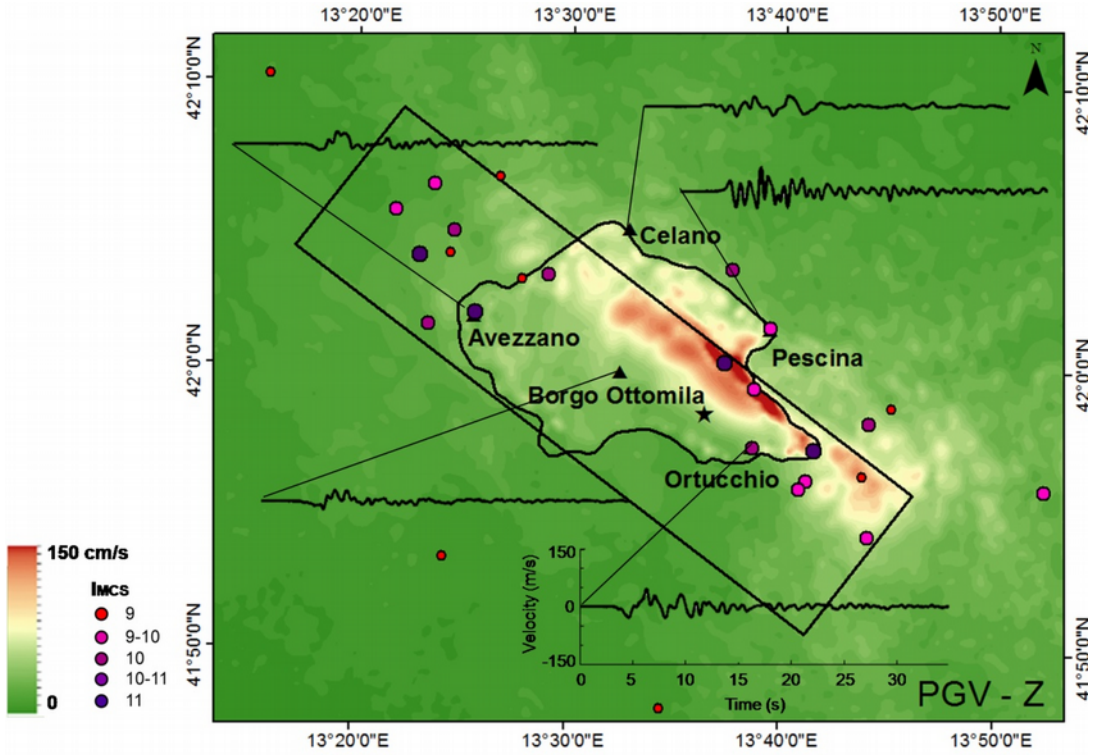

Fig. 11. PGV map for the Z component, in the same format as Fig. 8. Colored dots denote the I_{MCS} grades.

We have further explored in Fig. 12 the spatial variability of the ratio of vertical component with respect to the geometric mean of the horizontal ones (FN, FP) as a function of period, with reference to T = 0.75s, 1s, and 2s. Except for few cases, especially on the footwall side of the fault, where the tendency towards V/H ratios > 1 is apparent, low V/H ratios are confirmed within the basin, with average values around 0.5, in line with the observations from other earthquakes.

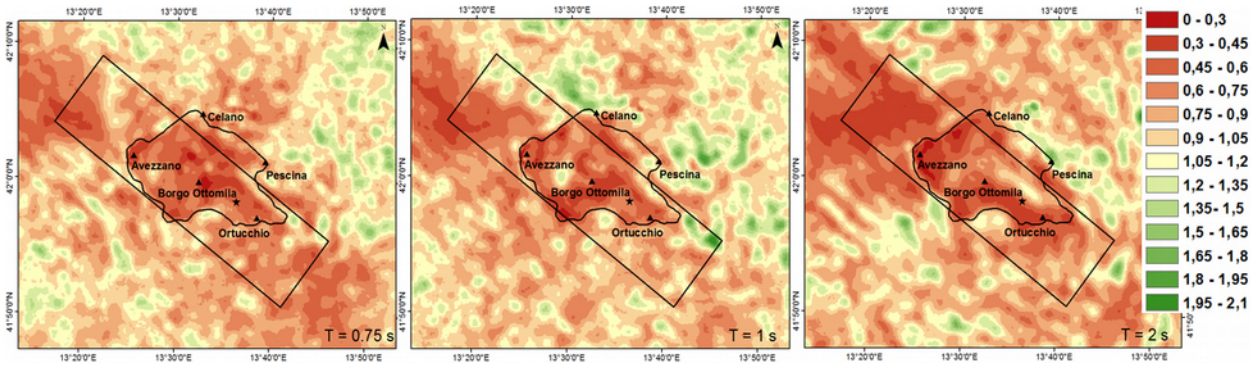

Fig. 12. Spatial distribution of the ratio between Z and the geometric mean of FN and FP components of 5% damped response acceleration spectrum for T = 0.75 s (a), 1 s (b), 2 s (c).

5.4 Comparison with GMPEs and considerations on the optimum distance metric in near-source

Comparison of our results with GMPEs is very instructive, not only in terms of peak values of motion, but also in terms of the corresponding spatial distribution. In Fig. 13, such a comparison is shown with the GMPE proposed by [36] based on Italian records (mostly from normal fault earthquakes) and the one by Cauzzi et al. [37], considering the closest distance from the fault rupture (R_{RUP}). The geometric mean of the horizontal components is considered.

Both GMPEs tend to underpredict results of the numerical simulations, but it is also clear that the adopted distance metric by [36], i.e., the Joyner-Boore distance (R_{JB}) from the surface projection of the fault, is not fit to properly describe the spatial distribution of ground motion in near-source conditions. As a matter of fact, by using the R_{JB} metric, all points on the surface fault projection are assigned by the GMPE the same peak value, irrespective of their actual position with respect to the fault rupture. This turns out to play a major role for those faults, either normal or reverse, with medium-to-low dip angles, for which a large surface projection of the fault is expected with a corresponding large variability of ground motion throughout that surface. A closer agreement with the spatial distribution of peak values is found instead in terms of the R_{RUP} distance metric considered by [37].

To explore further this subject, we have studied the spatial variability of simulated ground

motion considering different distance metrics, namely: R_{JB} (Joyner and Boore), R_{EPI} (epicentral), R_{HYP} (hypocentral), R_{RUP} (distance from the fault rupture), R_{RMS} (root-mean-square distance from the seismogenic part of the fault rupture plane, as defined by [38]). In addition to these classical distance metrics, we have also proposed the metric R_{LINE}, that is the closest distance from the surface fault projection of the segment at the top edge of the rupture plane. In this sense, R_{LINE} is similar to the R_X metric introduced by Chiou and Youngs [39], but in our work it is not used to discriminate between the hanging and footwall side of the fault, for the reasons explained in the following section. The actual position and length of the segment is set by projecting the hypocenter along the edge, and by considering it as the center of a segment of length given by the Wells and Coppersmith scaling relationships [40]. The resulting segment is shown on the left hand side map of Fig. 13.

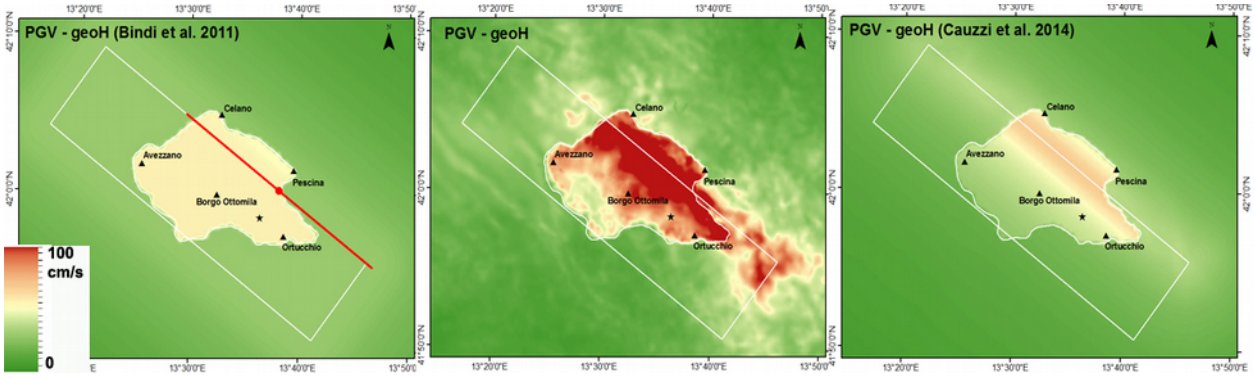

Fig. 13. Map of the computed Peak Ground Velocity (PGV). Geometric mean of the horizontal components obtained by SPEED (centre), by the GMPE proposed by Bindi et al. [36] in terms of R_{JB} (left), and by the GMPE proposed by Cauzzi et al. [37] in terms R_{RUP} (right).

Considering results in Fig. 14, for receivers up to about 40 km distance, the following comments can be made on the application of the different distance metrics for the study case:

- R_{EPI}: the scatter of results is very high and, more important, there is no tendency of decreasing amplitude with distance, since the epicenter lies away from the area of largest amplitude of ground motion;
- R_{HYP}: the limitation is similar as with R_{EPI}, with a scatter at short distances exceeding one order of magnitude;
- R_{JB}: a large number of points in this case lies at $R_{JB} \rightarrow 0$, that was set to a default value of 100 m for representation in a log scale. This implies a large scatter, similar as for R_{HYP}, which makes this distance metric hard to be used in near-source conditions. This was pointed out by other researchers, such as Roten et al. [41], who also noted the problems in using the R_{JB} metric in a similar environment of low-velocity sediments on the hanging wall side of a normal fault;
- R_{RUP}: a proper decrease of amplitude with distance can be found, with a lower scatter of results with respect to the previous cases. This may be considered as the best among the "classical" distance metrics typically used in the GMPEs to predict near-source ground motion;
- R_{LINE}: at short distance the scatter is significantly reduced, also because this metric is suitable to encompass, with the proper decay, different orders of magnitude of distance. At large distance, the scatter is similar to the other cases.
- R_{RMS}: the range of distance implied by this distance metric turns out to be limited, so that it cannot effectively capture the features of near-source ground motion for this case.

We can conclude that, in the case of a normal faulting earthquake, where differences between various distance metrics are far more pronounced than in a strike-slip earthquake or a near-vertical fault, the accuracy of prediction of ground motion in near-source conditions is critically dependent on the distance metric. From these numerical simulations, the distance from the fault rupture plane (R_{RUP}) turns out to be the best metric among the classical ones used for GMPEs, because it provides the proper decrease of amplitude with distance, with a reasonably reduced scatter. However, both the maps of PGV from numerical simulations, as well as the analysis of spatial variability from physics-based simulated ground motions, including also the recent experience with the May 29 2012 Po plain earthquake [28, 41], suggest that the best performance is obtained through the R_{LINE} distance, that has also the advantage of simplicity of calculation.

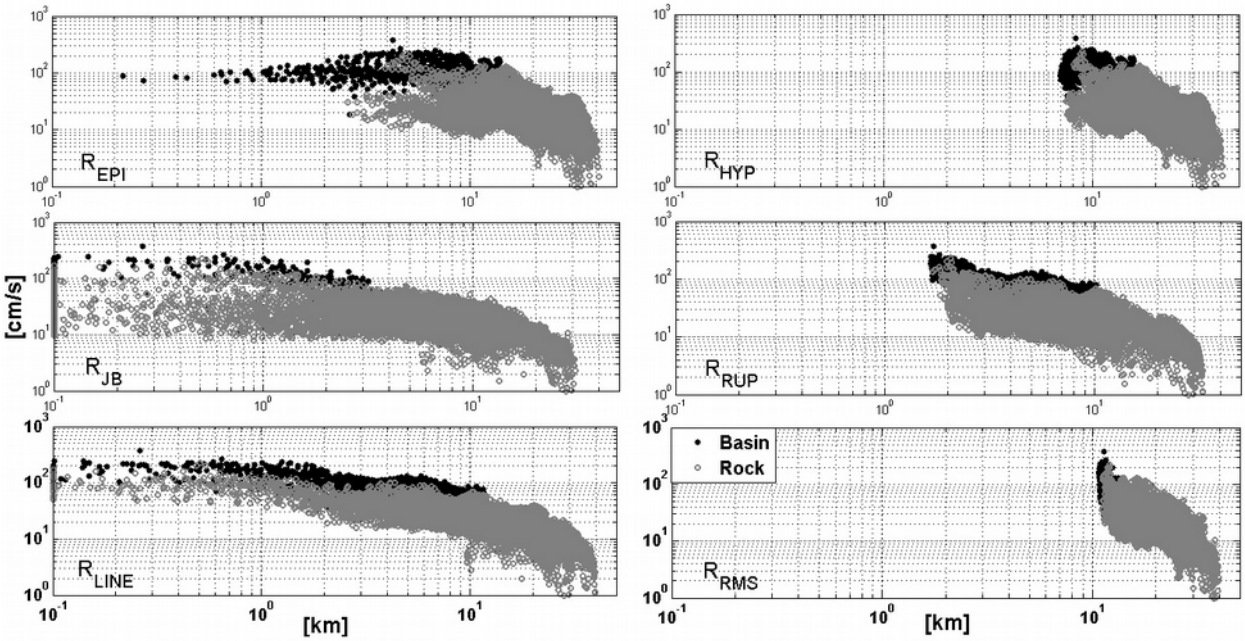

Fig. 14. Variability of PGV (FN component) with respect to different distance metrics. Values are expressed in cm/s.

5.5 Hanging wall vs footwall response

Influence of fault dip on the amplitude of earthquake ground motion in near-source conditions, and on its possible variation from the hanging to the foot wall sides of the fault (denoted by HW and FW, respectively) was the subject of several recent investigations. While for normal faulting, based on the relatively sparse amount of in situ observations (e.g., [43]) or of available records (e.g., [33]), the conclusion was drawn of the reduced amplitude of ground motion in the FW region, numerical simulations (e.g., [44]) suggest that such conclusion may hold only for low values of dip angle and that for dips larger than about 50° the situation tends to get opposite, with larger values on the FW side. The latter result is supported by our numerical simulations, the Marsica normal fault dipping about 53°, that show no significant dependency of results on the HW vs FW sides. This is suggested by the map in Fig. 8, showing a relatively homogeneous distribution of PGV, irrespective of the side

of the fault, but it is also more specifically demonstrated in Fig. 15, where the comparison is shown of the PGV (FN) on outcropping rock conditions, computed on the FW and HW sides, as a function of the R_{LINE} distance. It can be verified that the HW side is actually on average larger than the FW, but the difference is slight and may not be of practical relevance.

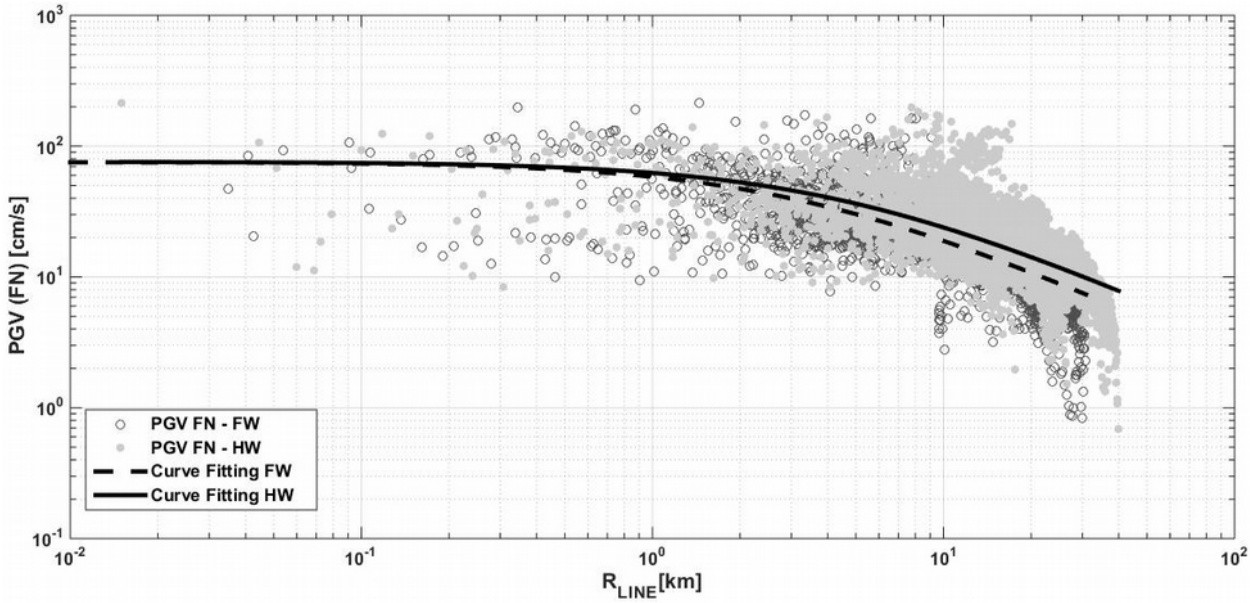

Fig. 15. Variability of PGV (FN component) with respect to R_{LINE} for points located on rock conditions on the hanging wall (HW) and on the footwall (FW) sides of the fault.

5.6 Evidence of 3D site effects in the basin amplification of seismic waves

We have explored the characteristics of the spatial variability of site amplification within the Fucino basin by first computing the 1D natural frequency f_0=Vs/4H, where H is the local thickness and Vs the average shear wave velocity to the bedrock. The resulting map of f_0 is shown in Fig. 16, and clearly portrays its low values, typically ranging from 0.2 to 0.8 Hz in the inner part of the basin, related to coupling low values of Vs to large sediment thickness.

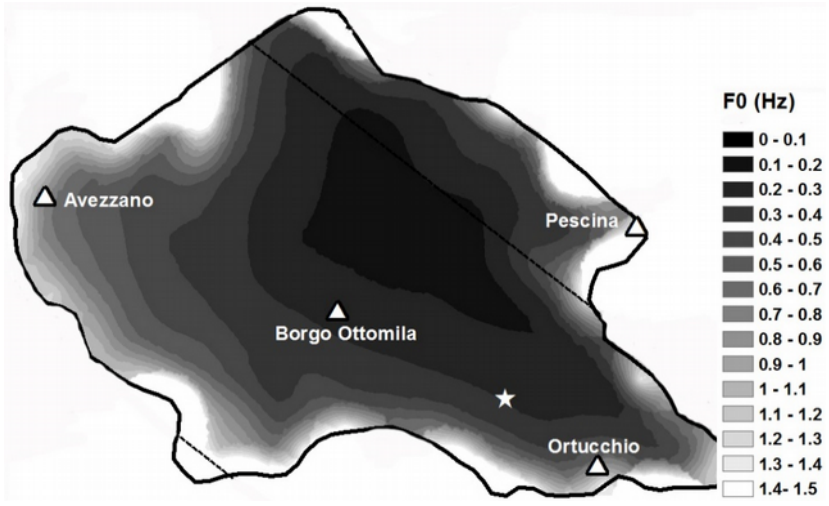

Fig. 16. Map of 1D natural frequency of vibration f_0 of the Fucino basin.

If the response of the Fucino basin were dominated by 1D amplification effects, we should expect that the response spectral ordinates at given locations be larger at periods close to $T=1/f_0$. To verify this argument, we have plotted in Fig. 17 the map of residuals $\varepsilon=\log_{10}(Sa_{sim}(R,T)/Sa_{avg}(R,T))$, where $Sa_{avg}(R,T)$ is the average simulated spectral ordinate at period T and at distance $R=R_{LINE}$, either within the basin or on rock, and $Sa_{sim}(R,T)$ is the corresponding value simulated at the specific location (geometric average of the horizontal components). Therefore, a positive value of ε means that the local site amplification at period T and distance R is larger than the average at the corresponding period and distance.

According to expectations from 1D modelling, these maps should roughly follow the spatial pattern of f_0 in Fig. 16. However, the pictures in Fig. 17 portray a much more complex feature of site amplification, with a broadband amplification in most sites within the inner portion of the basin (see e.g. Borgo Ottomila) and an irregular pattern at the edges. Consider for example the site of Avezzano, the main municipality of Marsica. In this case the residuals are positive both at short and long periods, implying a broadband amplification of ground motion, probably related to the unlucky combination of different effects, such as a) the directivity of the fault rupture propagation from the SE side of the fault towards NW; b) the amplification due to shallow layering and basin edge conditions, implying amplification at around T = 1 s and above, c) the NW propagation of long period surface waves amplified by the Fucino basin which are clearly prorayed by the snapshots of surface ground motion, especially along the FP component (see Fig. 7, right side). As a consequence, either because of the long period or because of the short period components of motion, such broadband amplification is probably the cause of the complete devastation of Avezzano during the 1915 earthquake.

We can conclude that, in a near-source environment such as studied in this work, the features of site amplification may be much more complex than predicted by classical 1D approaches, as also shown in [45] in a similar geological framework in Central Italy, and that they should be more properly evaluated with additional consideration of the basin and fault geometry and of the kinematic of slip along the fault.

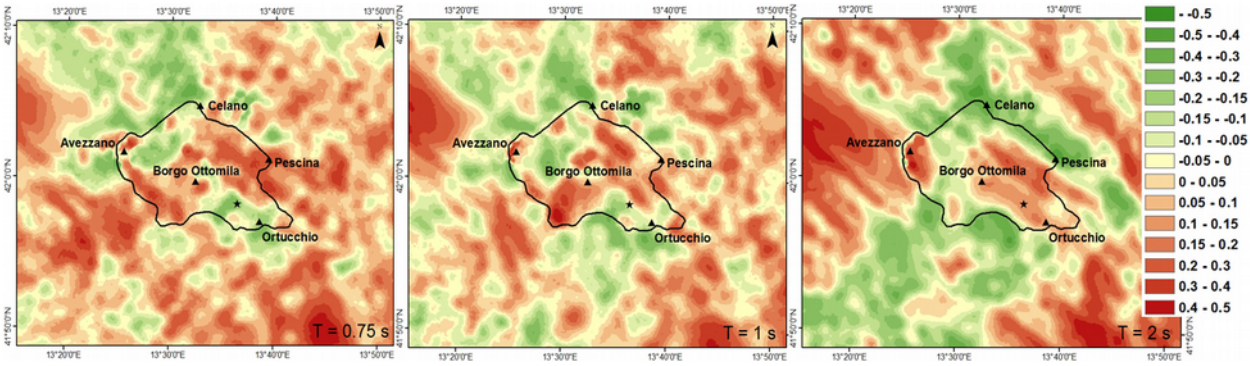

Fig. 17. Map of residuals $\varepsilon=\log_{10}(Sa_{sim}(R,T)/Sa_{avg}(R,T))$, where $Sa_{avg}(R,T)$ is the average simulated spectral ordinate at period T and at distance $R=R_{LINE}$, either within the basin or on rock, and $Sa_{sim}(R,T)$ is the corresponding value simulated at the specific location. Three values of period are considered: T= 0.75 s (a), 1 s (b), 2 s (c).

5.7 Other modelling assumptions: non linearity and 1D/3D layering

We finish this overview of 3D numerical results by addressing in Fig. 18 the comparison of results from three different runs using SPEED:

(a) the default run, that the numerical results presented in this paper refer to, consisting of the 3D numerical model of the Fucino basin and of the seismic fault (see Fig. 5), where a non-linear visco-elastic model, as described in section 2.2, was considered for soil materials (model 3DNL);
(b) the 3D linear visco-elastic model, with the same assumptions as in (a) as regards the numerical modelboth of the seismic fault and of the 3D basin stratigraphy (model 3DL);
(c) the 1D linear visco-elastic model, where, with respect to case (b), the geological model was approximated by a series of horizontal layers as in the crustal model of Table 1, where the first 300 m were replaced by a single layer with Vs = 300 m/s, to represent average conditions within the Fucino basin (model 1DL).

As it can be seen from Figure 18, limited to the FP component of velocity, both 3DL and 3DNL models tend to provide larger values than 1DL, the first ones being affected by a much larger complexity of ground motion. For instance, in Avezzano the peak amplitude is nearly twice that provided by the 1DL model, probably because of constructive interference of body waves and the train of surface waves generated within the basin. The effect of the NL model is evident both in the reduction of the ground motion amplitude and of a slight delay in the phases, because of the temporary decrease of the shear wave velocity, but also in the reduction of the large reverberation effects inside the basin. Note that the NL elastic model does not imply any permanent degradation of the soil properties, at variance with the classical linear equivalent approaches, because the initial conditions are completely recovered.

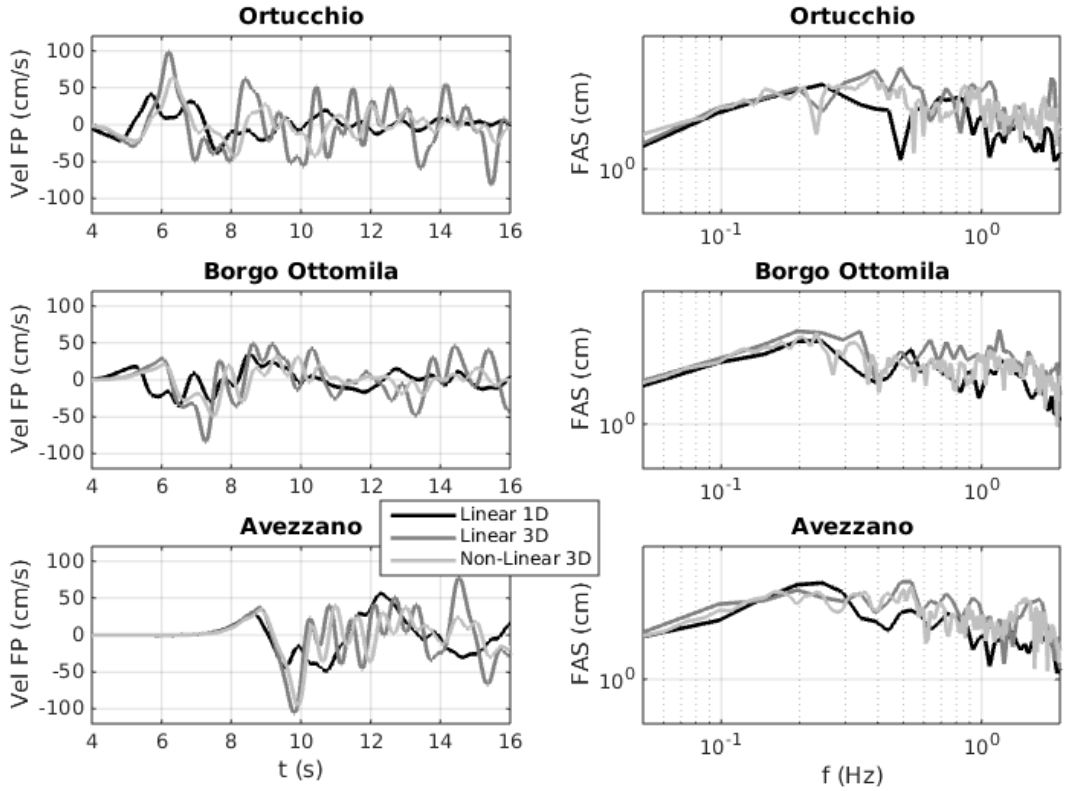

Fig. 18. Comparison of FP velocity time histories (left) and of the corresponding Fourier spectra (right) simulated at Ortucchio (top), Borgo Ottomila (middle) and Avezzano (bottom) with the modelling assumptions 3DNL, 3DL and 1DL, described in the text.

6. Conclusions

This paper presented an overview of results of the 3D physics-based numerical simulations of the 1915 Marsica earthquake, which devastated Avezzano and surrounding villages, causing more than 33,000 fatalities. Results matched reasonably well some post-earthquake observations, such as the geodetic measurements of co-seismic vertical ground displacements, found to be consistent with a M_W 6.7 earthquake magnitude, and the estimated prevailing directions of shaking. Furthermore, they provided a realistic picture of earthquake ground motion in a condition, quite common in Central Apennines, where there may be a strong interaction of near-source conditions with the complex geology associated to the presence, within an extensional environment, of shallow tectonic basins with relatively soft-soil sediments.

A large variability of earthquake ground motion within such a complex geological and tectonic configuration, both in terms of amplitude and prevailing features, was highlighted by this study, in line with the report of Oddone [4], who, in his strikingly in-depth survey of the consequences of the earthquake based on the failures of structures and interviews to survivors, found clear evidence and witnesses of "all imaginable types of motion", from vertical, to horizontal, to rocking. A complexity hard to be predicted by standard engineering tools based on 1D shear wave propagation, such as demonstrated by the features of ground

motion amplification and of the spatial distribution of the fault normal, fault parallel and vertical components.

In such complex near-source conditions, recent GMPEs may lead to underestimations of the earthquake ground motion amplitude, since they are rather poorly constrained because of scarcity of records. Furthermore, a careful choice should be made in terms of distance metric: among the classical metrics, R_{RUP} turns out to be the best one, but the metric R_{LINE}, introduced in this work, provides even better performance than R_{RUP}. No significant differences were found between hanging and footwall sides of the fault, in agreement with the numerical findings presented by [44], for the normal fault condition, with relatively large dip angle, examined in this study.

The impact of different modelling assumptions was also explored, which highlighted, on the one side, the relevance of the 3D numerical modelling of such a complex geological configuration, and, on the other side, the role of the non-linear constitutive modelling of the soil materials, as already pointed out by other research works on 3D physics-based numerical simulations (e.g., [46]). In spite of its simplicity, the non-linear elastic model considered in this work is suitable to provide more realistic results than the linear assumption under such large values of ground motion, with a relatively minor impact on the computational performance of the code.

We can finally conclude that the numerical approaches and computational tools for 3D physics-based simulations are becoming more and more suitable to provide realistic ground shaking scenarios of past and future earthquakes, and are expected to provide in the next future an effective support to real records, to improve reliability of predicting tools of earthquake ground motions and seismic hazard evaluations.

Acknowledgments

This work was stimulated by the invitation received by the first author from Fabrizio Galadini, INGV, to present a lecture at the conference in Avezzano to commemorate the centennial from the earthquake. Fabrizio Galadini and Gianluca Valensise, INGV, provided useful comments and research material that was used to better constrain the numerical model. Funding from the DPC-RELUIS Project RS2, on Numerical simulations and near-source effects, is also gratefully acknowledged. Ilario Mazzieri was partially supported by the research grant no. 2015-0182 “PolyNum: Polyhedral numerical methods for partial differential equations” funded by Fondazione Cariplo and Regione Lombardia. In-depth comments by two anonymous reviewers were very beneficial to improve the quality of and results of the paper.

References

[1] Guidoboni E, Ferrari G, Mariotti D, Comastri A, Tarabusi G, Valensise G. CFTI4Med, Catalogue of Strong Earthquakes in Italy (461 B.C.-1997) and Mediterranean Area (760 B.C.-1500). INGV-SGA 2007. Available at http://storing.ingv.it/cfti4med/ (Last access: May 2015).

[2] Galadini F, Galli P. The Holocene paleoearthquakes on the 1915 Avezzano earthquake faults (central Italy): Implications for active tectonics in Central Apennines. Tectonophysics 1999; 308: 143-170.

[3] Galli P, Messina P, Giaccio B, Peronace E, Quadrio B. Early Pleistocene to late Holocene activity of the Magnola fault (Fucino fault system, central Italy). Boll. Geof. Teorica ed Applicata 2012; 53: 435-458.

[4] Oddone E. Gli elementi fisici del grande terremoto marsicano fucense del 13 Gennaio 1915. Bollettino della Società Sismologica Italiana 1915; 29: 71-215 [in italian].

[5] Basili A, Valensise G. Contributo alla caratterizzazione della sismicità dell'area marsicano-fucense. in Proc. II Workshop on "Aree Sismogenetiche e Rischio Sismico in Italia", E. Boschi and M. Dragoni (eds) Erice 1986; 197-214 [in italian].

[6] Favali P and Frugoni F. Revisione critica dei parametri fisici del terremoto. In: "13 gennaio 1915. Il terremoto nella Marsica" a cura di S. Castenetto e F. Galadini 1999; 273-282 [in italian].

[7] Cavinato GP, Carusi C, Dall'Asta M, Miccadei E, Piacentini T. Sedimentary and tectonic evolution of Plio-Pleistocene alluvial and lacustrine deposits of Fucino basin (Central Italy). Sedimentary Geology 2002; 148: 29-59.

[8] Giraudi C. Evoluzione geologica tardo pleistocenica ed olocenica della Piana del Fucino e dei versanti adiacenti: analisi di nuovi dati stratigrafi ci e radiometrici e ricostruzione delle variazioni ambientali. In 13 Gennaio 1915. Il terremoto della Marsica (a cura di Castenetto S. e Galadini F.). C.N.R., Serv. Sis. Naz., Ist. Poligr. Stat. Roma 1999; 183-197 [in italian].

[9] Locati M, Camassi R, Stucchi M. DBMI11, la versione 2011 del Database Macrosismico Italiano 2011. Milano, Bologna. Available at http://emidius.mi.ingv.it/DBMI11. DOI: 10.6092/INGV.IT-DBMI11.

[10] Cavinato GP, De Celles PG. Extensional basins in the tectonically bimodal central Apennines fold-thrust belt, Italy: response to corner flow above a subducting slab in retrograde motion. Geology 1999; 27 (10): 955-958.

[11] Cara F, Di Giulio G, Cavinato GP, Famiani, Milana G. Seismic characterization and monitoring of Fucino Basin (Central Italy). Bull. Earthquake Eng 2011; 9:1961-1985.

[12] Pane V, Burghignoli A. Determinazione in laboratorio delle caratteristiche dinamiche dell'argilla del Fucino. CNR Atti del Convegno del Gruppo Nazionale di Coordinamento per gli Studi di Ingegneria Geotecnica, Monselice 1988; 1:115-139 [in italian].

[13] Stupazzini M, Paolucci R, Igel H. Near-fault earthquake ground-motion simulation in the Grenoble valley by a high-performance spectral element code. Bulletin of the Seismological Society of America 2009; 99(1): 286–301.

[14] Ameri G, Gallovic F, Pacor F. Complexity of the Mw 6.3 2009 L'Aquila (central Italy) earthquake: 2. Broadband strong motion modeling. Journal of Geophysical Research 2012; 117, B04308.

[15] Working Group MS–AQ. Microzonazione sismica per la ricostruzione dell'area aquilana vol. 3 and Cd-rom. L'Aquila: Regione Abruzzo – Dipartimento della Protezione Civile 2010.

[16] Ward SN, Valensise G. Fault parameters and slip distribution of the 1915 Avezzano, Italy, earthquake derived from geodetic observations. Bulletin of the Seismological Society of America 1989; 79: 690–710.

[17] Berardi R, Mendez A, Mucciarelli M, Pacor F, Longhi G, Petrungaro C. On the modelling of strong motion parameters an correlation with historical macroseismic data: an application to the 1915 Avezzano earthquake. Annali di Geofisica 1995; 38: 851-866.

[18] Amoruso A, Crescentini L, Scarpa R. Inversion of source parameters from near and far-field observations: an application to the 1915 Fucino earthquake, Central Apennines, Italy. Journal of Geophysical Research 1998; 103(B12): 29,989-29,999.

[19] Galadini F, Galli P, Giraudi C. Geological investigations of Italian earthquakes: new paleoseismological data from the Fucino plain (Central Italy). Journal of Geodynamics 1997; 24:87-103.

[20] Schiappapietra E. 13 gennaio 1915. Il terremoto della Marsica. Simulazioni numeriche 3D del moto in campo near-source. Msc Thesis in Environmental Engineering, 2015 Politecnico di Milano (in Italian)

[21] Antonietti PF, Mazzieri I, Quarteroni A, Rapetti F. Non-conforming high order approximations of the elastodynamics equation. Computer Methods in Applied Mechanics and Engineering 2012; 209-212: 212 – 238.

[22] Faccioli E, Maggio F, Paolucci R, Quarteroni A. 2D and 3D elastic wave propagation by a pseudo-spectral domain decomposition method. Journal of Seismology 1997; 1(3): 237–251.

[23] Komatitsch D and Tromp J. Introduction to the spectral-element method for 3-D seismic wave propagation. Geophysical Journal International 1999; 139(3): 806–822.

[24] Paolucci R, Mazzieri I, Smerzini C, Stupazzini M. Physics-based earthquake ground shaking scenarios in large urban areas. in Perspectives on European Earthquake Engineering and Seismology, Geotechnical, Geological and Earthquake Engineering ed. Ansal, A., Springer 2014; 34: Chapter 10, 331-359.

[25] Moczo P, Kristek J, Galis M. The Finite-Difference Modelling of Earthquake Motions: Waves and Ruptures. Cambridge University Press 2014.

[26] Stacey R. Improved transparent boundary formulations for the elastic-wave equation. Bulletin of the Seismological Society of America, 1988; 78(6): 2089–2097.

[27] Butcher JC. Numerical Methods for Ordinary Differential Equations, 2nd Edition,Wiley, 2008.

[28] Paolucci R, Mazzieri I, Smerzini C. Anatomy of strong ground motion: near-source records and 3D physics-based numerical simulations of the Mw 6.0 May 29 2012 Po Plain earthquake, Italy. Geophysical Journal International, 2015; 203: 2001–2020.

[29] Mazzieri I, Stupazzini M, Guidotti R, Smerzini C. SPEED: SPectral Elements in Elastodynamics with Discontinuous Galerkin: a non-conforming approach for 3D multi-scale problems. International Journal for Numerical Methods in Engineering 2013; 95(12): 991–1010.

[30] Smerzini C, Villani M. Broadband Numerical Simulations in Complex Near-Field Geological Configurations: The Case of the 2009 Mw 6.3 L'Aquila Earthquake. Bulletin of the Seismological Society of America 2012; 102: 2436–2451.

[31] Herrero A, Bernard P. A kinematic self-similar rupture process for earthquakes. Bulletin of the Seismological Society of America 1994; 84(4):1216–1228

[32] Loperfido A. Indagini astronomico-geodetiche relative al fenomeno sismico della Marsica. Atti Minist. Lavori Pubblici, Florence, Italy 1919; 95 pp. [in italian].

[33] Anderson JG, Kawase H, Biasi GP, Brune JN, Aoi S. Ground Motions in the Fukushima Hamadori, Japan, Normal-Faulting Earthquake. Bulletin of the Seismological Society of America 2013; 103: 1935–1951.

[34] Gülerce Z. and N.A. Abrahamson. Site-Specific Design Spectra for Vertical Ground Motion. Earthquake Spectra 2011; 27: 1023–1047.

[35] Ambraseys, N. N., and Douglas, J. Near field horizontal and vertical earthquake ground motions. Soil Dynamics and Earthquake Engineering 2003; 23: 1–18.

[36] Bindi D, Pacor F, Luzi L, Puglia R, Massa M, Ameri G, Paolucci R. Ground motion prediction equations derived from the Italian strong motion database. Bull Earthquake Eng. 2011; 9:1899–1920.

[37] Cauzzi C, Faccioli E, Vanini M, Bianchini A. Updated predictive equations for broadband (0.01–10 s) horizontal response spectra and peak ground motions, based on a global dataset of digital acceleration records. Bulletin of Earthquake Engineering, 2014; 13(6): 1587-1612.

[38] Scherbaum F, Cotton F, Staedtke H. The Estimation of Minimum-Misfit Stochastic Models from Empirical Ground-Motion Prediction Equations. Bulletin of the Seismological Society of America, 2006; 96 (2): 427—445.

[39] Chiou BSJ, Youngs RR. An NGA Model for the Average Horizontal Component of Peak Ground Motion and Response Spectra. Earthquake Spectra 2008; 24:173–215.

[40] Wells DL, Coppersmith KJ. New Empirical Relationships among Magnitude, Rupture Length, Rupture Width, Rupture Area, and Surface Displacement. Bulletin of the Seismological Society of America 1994; 84: 974–1002.

[41] Roten D, Olsen KB, Pechmann, JC, Cruz-Atienza VM, Magistrale H. 3D Simulations of M 7 Earthquakes on the Wasatch Fault, Utah, Part I: Long-Period (0-1 Hz) Ground Motion. Bulletin of the Seismological Society of America, 2011; 101(5): 2045-2063.

[42] Hashemi K., Mazzieri I, Paolucci R, Smerzini C. Spatial Variability of Near-Source Seismic Ground Motion with respect to different Distance Metrics. 7th Int. Conf. on Seismology and Earthquake Engineering, Tehran, 2015, Paper n. 770-SM.

[43] Brune JN. Precarious rock evidence for low ground shaking on the footwall of major normal faults. Bulletin of the Seismological Society of America, 2000; 90: 1107–1112.

[44] O'Connell RHD, Ma S, Archuleta RJ. Influence of Dip and Velocity Heterogeneity on Reverse- and Normal-Faulting Rupture Dynamics and Near-Fault Ground Motions. Bulletin of the Seismological Society of America 2007; 97(6): 1970-1989

[45] Smerzini C, Paolucci R, Stupazzini M. Comparison of 3D, 2D and 1D numerical approaches to predict long period earthquake ground motion in the Gubbio plain, Central Italy. Bulletin of Earthquake Engineering, 2011, 9:2007–2029.

[46] Taborda R, Bielak J, Restrepo D. Earthquake Ground-Motion Simulation including Nonlinear Soil Effects under Idealized Conditions with Application to Two Case Studies. Seismological Research Letters 2012; 83(6): 1047-1060.

MOX Technical Reports, last issues

Dipartimento di Matematica
Politecnico di Milano, Via Bonardi 9 - 20133 Milano (Italy)

51/2016 Guzzetti, S.; Perotto, S.; Veneziani, A.
Hierarchical Model Reduction for Incompressible Flows in Cylindrical Domains: The Axisymmetric Case

48/2016 Scardulla, S.; Pasta, S.; D'Acquisto, L.; Sciacca, S.; Agnese, V.; Vergara, C.; Quarteroni, A.; C
Shear Stress Alterations in the Celiac Trunk of Patients with Continuous-Flow Left Ventricular Assist Device by In-Silico and In-Vitro Flow Analysis

49/2016 Formaggia, L.; Scotti, A.; Sottocasa, F.
ANALYSIS OF A MIMETIC FINITE DIFFERENCE APPROXIMATION OF FLOWS IN FRACTURED POROUS MEDIA

50/2016 Ambrosi, D.; Pezzuto, S.; Riccobelli, D.; Stylianopoulos, T.; Ciarletta, P.
Solid tumors are poroelastic solids with a chemo--mechanical feedback on growth

46/2016 Lila, E.; Aston, J.A.D.; Sangalli, L.M.
Smooth Principal Component Analysis over two-dimensional manifolds with an application to Neuroimaging

47/2016 Canuto, C.; Nochetto, R. H.; Stevenson R.; Verani, M.
On p-Robust Saturation for hp-AFEM

45/2016 Bukac, M.; Yotov, I.; Zunino, P.
DIMENSIONAL MODEL REDUCTION FOR FLOW THROUGH FRACTURES IN POROELASTIC MEDIA

44/2016 Notaro, D.; Cattaneo, L.; Formaggia, L.; Scotti, A.; Zunino, P.
A Mixed Finite Element Method for Modeling the Fluid Exchange between Microcirculation and Tissue Interstitium

43/2016 Ambrosi, D.; Ciarletta, P.; De Falco, C.; Taffetani, M.; Zunino, P.
A multiscale modeling approach to transport of nano-constructs in biological tissues

42/2016 Iannetti, L.; D'Urso, G.; Conoscenti, G.; Cutri, E.; Tuan, R.S.; Raimondi, M.T.; Gottardi, R.; Z
Distributed and lumped parameter models for the characterization of high throughput bioreactors